



HAL
open science

Synthesis and characterization of thermally treated $\text{Co}_{1-x}\text{Fe}_2+x\text{O}_4$ ($x = 0.0 - 0.8$) spinel nano ferrite

C Parmar, R Verma, S S Modak, Frédéric Mazaleyrat, S N Kane

► **To cite this version:**

C Parmar, R Verma, S S Modak, Frédéric Mazaleyrat, S N Kane. Synthesis and characterization of thermally treated $\text{Co}_{1-x}\text{Fe}_2+x\text{O}_4$ ($x = 0.0 - 0.8$) spinel nano ferrite. International Conference on Materials Science and Manufacturing Technology (ICMSMT 2022), Apr 2022, Coimbatore, India. pp.012009, 10.1088/1757-899x/1258/1/012009 . hal-04013009

HAL Id: hal-04013009

<https://hal.science/hal-04013009v1>

Submitted on 3 Mar 2023

HAL is a multi-disciplinary open access archive for the deposit and dissemination of scientific research documents, whether they are published or not. The documents may come from teaching and research institutions in France or abroad, or from public or private research centers.

L'archive ouverte pluridisciplinaire **HAL**, est destinée au dépôt et à la diffusion de documents scientifiques de niveau recherche, publiés ou non, émanant des établissements d'enseignement et de recherche français ou étrangers, des laboratoires publics ou privés.



Distributed under a Creative Commons Attribution 4.0 International License

PAPER • OPEN ACCESS

Synthesis and characterization of thermally treated $\text{Co}_{1-x}\text{Fe}_{2+x}\text{O}_4$ ($x = 0.0 - 0.8$) spinel nano ferrite

To cite this article: C Parmar *et al* 2022 *IOP Conf. Ser.: Mater. Sci. Eng.* **1258** 012009

View the [article online](#) for updates and enhancements.

You may also like

- [The influence of cation stoichiometry on the critical currents and the phase formation in Ag-sheathed Bi\(2223\) tapes](#)
M Quilitz, A Arce and W Goldacker
- [Impact of Different Yearly Rainfall Patterns on Dynamic Changes of Soil Moisture of Fixed Sand Dune in the Horgin Sandy Land](#)
Shuxia Yao and Chuancheng Zhao
- [Discrete-Dopant-Fluctuated Transient Behavior and Variability Suppression in 16-nm-Gate Complementary Metal-Oxide-Semiconductor Field-Effect Transistors](#)
Yiming Li, Chih-Hong Hwang and Hui-Wen Cheng



The Electrochemical Society
Advancing solid state & electrochemical science & technology

243rd ECS Meeting with SOFC-XVIII

More than 50 symposia are available!

Present your research and accelerate science

Boston, MA • May 28 – June 2, 2023

[Learn more and submit!](#)

Synthesis and characterization of thermally treated $\text{Co}_{1-x}\text{Fe}_{2+x}\text{O}_4$ ($x = 0.0 - 0.8$) spinel nano ferrite

C Parmar¹, R Verma¹, S S Modak², F Mazaleyrat³ and S N Kane^{1,*}

¹Magnetic Materials Laboratory, School of Physics, D. A. University, Khandwa road, Indore-452001, India

²Physics Department, Jaypee University of Engineering and Technology, Raghogarh, Guna 473226, India

³SATIE, ENS Paris-Saclay, 4 Avenue des Sciences, 91190 Gif-sur-Yvette, France

*E-mail: kane_sn@yahoo.com(S. N. Kane)

Abstract. We report the effect of surplus-Fe-content, and thermal annealing on the properties of sol gel auto-combustion synthesized $\text{Co}_{1-x}\text{Fe}_{2+x}\text{O}_4$ ($x = 0.0-0.8$) spinel ferrites. X-ray diffraction (XRD), magnetic measurements, Fourier transform infrared (FTIR) spectroscopy, Ultraviolet-visible (UV-Vis) are used to monitor the effect of excess Fe-content, and thermal annealing dependence of properties, and correlation among them. XRD validates presence of spinel nanoferrite (31.54 – 44.89 nm) phase, minor presence of $\alpha\text{-Fe}_2\text{O}_3$ phase was also detected. Results reveal that variation of Fe-content leads to: i) variation of lattice-parameter, re-distribution of Fe^{3+} , Co^{2+} ions on A, B-site, ii) alteration of inversion degree, disorder, iii) modification of saturation magnetization due to spin disorder at surface, iv) variation of coercivity, and related grain size imply that studied ferrites are in single-multi domain overlap regions, while squareness-ratio indicates variation of inter-grain interaction, isotropic behaviour of multi-domain particles; iv) fine-tuning of bandgap (1.35 – 1.5 eV) via changes in cationic-distribution and lattice-parameter, v) variation of Debye temperature, suggests modification of lattice vibrations. Current work implies strong correlation between bandgap magnetic, structural properties.

1. Introduction

Ferrimagnetic spinel-ferrites are represented by formula $\text{Me}^{2+}\text{O}.\text{Fe}^{3+}_2\text{O}_3$, display face centred cubic 'fcc' structure, with Fd_3m space group, and have two inter-penetrating sub-lattices tetrahedral (A), octahedral (B) [1, 2, 3]. Ferrites are vital materials for their use in microwave devices, high frequency devices, etc. For their usage in various devices, magnetic properties should to be optimized [4, 5]. By choosing: i) a particular method: e.g. – sol gel [6, 7], hydrothermal [8], solid state reaction [9], co-precipitation [10] etc., ii) compositional variation [6, 7, 11], and iii) thermal annealing /or no thermal annealing [12], ion irradiation [13] etc. Literature also reports tuning of bandgap, structural, magnetic properties [14, 15, 16]. CoFe_2O_4 has inverse spinel structure, and Fe^{3+} ions are dispersed nearly equally on A (tetrahedral), B (octahedral) site, while Co^{2+} ions on B site. Although, CoFe_2O_4 is a well studied ferrite, exhibits interesting properties including excellent chemical stability, high Curie temperature, high saturation magnetization, coercivity [17], and widely used in electronic devices, magnetic-resonance-imaging (MRI) [18, 19], targeted drug delivery, for cancer treatment (hyperthermia) [20], transformer cores, high density storage devices, magnetic fluids, , humidity, and



gas sensors, etc. [4, 21]. However, studies on influence of excess amount of Fe (*where there is excess Fe i.e. more than 2*) in Co-based $\text{Co}_{1-x}\text{Fe}_{2+x}\text{O}_4$ -type spinel ferrites are less reported [22]. $\text{Co}_{0.8}\text{Fe}_{2.2}\text{O}_4$ system (*here excess Fe is 0.2*), reported in [22] shows magnetic field induced phase transition [23]. Kane et al [14] report the study of bandgap, magnetic, structural, properties, in dry gel $\text{Co}_{1-x}\text{Fe}_{2+x}\text{O}_4$ ($x = 0.0-0.8$) spinel nano ferrites, where excess Fe-content has considerable effect on aforementioned properties. In spinel ferrites, compositional variation, thermal annealing etc. is known to affect structural, magnetic properties, bandgap e. g. – [6, 7, 11, 14, 24] etc. So study of effect of thermal annealing in $\text{Co}_{1-x}\text{Fe}_{2+x}\text{O}_4$ ($x = 0.0-0.8$) spinel ferrite, would be interesting to obtain the information on thermal annealing induced changes in structural, magnetic properties, bandgap and correlation between them.

Thus, objective of the present work is to study the influence of surplus-Fe-content, and thermal annealing on the properties of sol gel autocombustion synthesized $\text{Co}_{1-x}\text{Fe}_{2+x}\text{O}_4$ ($x = 0.0-0.8$) spinel ferrites. Effect of excess Fe-content, and thermal annealing dependence of properties was monitored by XRD, magnetic measurements, UV-Vis, FTIR spectroscopy.

2. Material synthesis, material characterization, and data analysis

Preparation of $\text{Co}_{1-x}\text{Fe}_{2+x}\text{O}_4$ ($x = 0.0 - 0.8$) spinel nano ferrites was done by sol-gel autocombustion method, utilizing AR grade nitrate-citrate precursors, During synthesis solution pH was maintained at 7, by adding Ammonia solution $[\text{NH}_4\text{OH}]$, and metal salt to citric acid ratio was kept as 1:1. More details on synthesis can be seen in [14]. Prepared dry gel samples were annealed in muffle furnace (in air) at 600 °C for 3 hours, and were used for characterization.

Structural characterization of the samples was done at room temperature by X-ray diffraction (XRD) measurements using Bruker D8 diffractometer utilizing $\text{Cu-K}\alpha$ radiation (wavelength ' λ ' = 0.1541 nm) in $\theta - 2\theta$ configuration (step size: 0.02°). Vibrating sample magnetometer (Lake Shore 7310 model), at room temperature was used to get magnetization measurements. Room temperature Ultraviolet-Visible (UV-Vis) measurements (in reflection mode) were done by Perkin-Elmer spectrometer (Model: Lamda 950) to get the bandgap. Absorption mode Fourier transmission infrared (FTIR) measurements (in KBr matrix) were done by Perkin Elmer spectrometer.

MAUD (Material Analysis Using Diffraction), Reitveld refinement software [25] is employed to get full profile analysis of the XRD pattern, which also verified the formation of fcc spinel phase. Analysis of XRD data as described in [6, 26, 27], yields structural parameters: lattice parameter (a_{exp}), Scherrer's grain diameter (D_S), X-ray density (ρ_{XRD}), specific surface area (S), dislocation density (ρ_D). Using X-ray diffraction line intensities, cationic distribution of each composition was estimated via employing Bertaut method [27, 28], was used to compute theoretical lattice parameter (a_{th}), oxygen parameter (u), inversion parameter (δ), Néel magnetic moment ' n_N ' or ' $M_{S(th)}$ ' (theoretical magnetization at 0 K) and, canting angle (α_{Y-K}) [27]. Hysteresis loops were used to obtain coercivity (H_c), saturation magnetization (M_S), reduced remanence (M_r/M_S) anisotropy constant (K_1). Energy bandgap was computed by using Kubelka-Munk (K-M) function via following equations: $F(R) = [1 - R^2] / 2R$, and $\alpha h\nu = A (h\nu - E_g)^n$, where R – reflectance and $F(R)$ is Kubelka-Munk function, is proportional to incorporation of the adsorbate molecules, while $h\nu$, α , A , and n represent respectively the energy of the photon, the absorption coefficient, the material parameter, and E_g – the bandgap [14, 27, 29]. FTIR data was analyzed to obtain absorption band positions, force constants for tetrahedral, octahedral sites (K_T , K_O), and Debye temperature (θ_D). Error shown in table(s), figure(s) is '*Standard Deviation*' obtained from the data.

3. Results and discussions

X-ray diffractograms of the studied samples are shown as figure 1 (a), confirm the formation of nano-crystalline (grain diameter: 31.54 nm to 44.89 nm) cubic spinel structure. Small fraction of Fe_2O_3 was also detected, ascribed to moderate thermal annealing temperature: 600 °C, as was also observed earlier [27, 30]. Figure 1 (b) illustrates the representative Rietveld refined plot for $x = 0.2$ sample. Figure 2 (a) shows compositional dependence of Scherrer's grain diameter ' D_S ', while inset depicts

variation of $a_{exp.}$. Based on compositional dependence of D_S , $a_{exp.}$, following experimental relations can be written: i) $D_S = 44.90268 - 16.68858$ [Fe content], ii) $a_{exp.} = 0.83852 - 0.00313$ [Fe content]. Aforementioned experimental relations show association among composition, and structural parameters: D_S , $a_{exp.}$. Observed variation of $a_{exp.}$ is ascribable to slight variation of ionic radii of Co^{2+} (0.065 nm), and Fe^{3+} (0.067 nm), and allocation of Fe, Co ions on A, B site (see table 1), as was also reported earlier [14] where minor changes in $a_{exp.}$ were observed, and no thermal treatment was used. Agreement between theoretical lattice parameter $a_{th.}$ (range between: 0.8306 – 0.8414 nm), and $a_{exp.}$ (0.8354 – 0.8390 nm), shows that obtained cationic distribution (see table 1) is close to actual one. Observed grain diameter (range between 31.54 – 44.89 nm) values are higher as compared to earlier report (range between 28.26 – 36.67 nm) [14], are ascribable to annealing assisted growth of grains [31]. Figure 2 (b) depicts the compositional dependence of dislocation density, ascribable to compositional dependent variation of Fe, Co ions allocation on site A, B (shown in table 1). Figure 2(b) inset depicts grain diameter dependence of ρ_D . Based on figure 2, and its inset, the following experimental relations are written, showing strong correlation between composition, and structural parameters: i) $\rho_D = 0.47215 + 0.623$ [x], and ii) $\rho_D = 24.85 \exp.(-D_S/6.17) + 3.99 \exp.(-D_S/18.66) + 0.12$.

Table 1 depicts the cation distribution, oxygen parameter (u), inversion parameter (δ), theoretical lattice parameter ($a_{th.}$), specific surface area (S), and x-ray density (ρ_{XRD}). Table 1 shows that ρ_{XRD} range between 5272.17 – 5297.48 kg/m³, shows that with reducing Co-content, there is a shrinkage of unit cell (evidenced by reduction of $a_{exp.}$) leading to increase of ρ_{XRD} , which is slightly higher than ρ_{XRD} values reported in earlier work [14], where ρ_{XRD} varies between 5268.99 – 5292.15 kg/m³. Observed higher ρ_{XRD} values are ascribable to thermal annealing. Specific surface area (S) varies between 25.35 – 36.08 m²/g, which is higher than as reported in [14]: 16.23 30.03 m²/g. Higher S value is useful for heterogeneous catalysis, owing to the higher surface area. Table 1 shows that thermal annealing leads to re-distribution of cations (Co^{2+} , Fe^{3+}) on site A, B, affecting degree of inversion (δ) revealing mixed

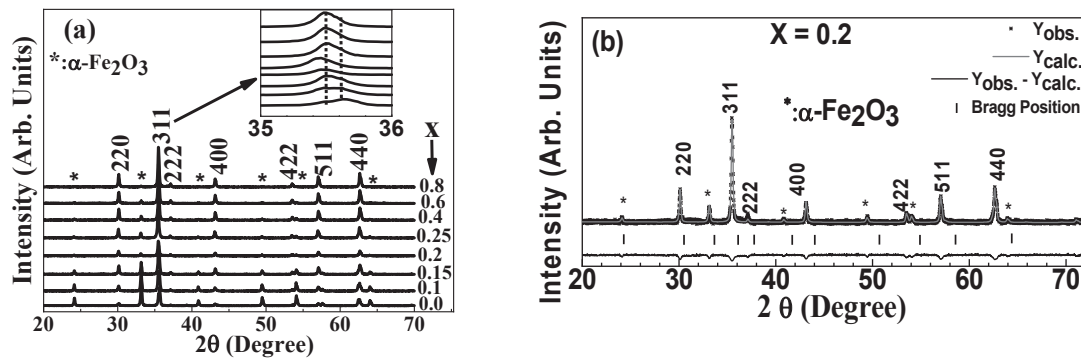


Figure 1. (a) XRD patterns of $Co_{1-x}Fe_{2+x}O_4$ samples, Inset: zoom part of (311) peak, where peak shift is shown by dotted lines, (b) Representative Rietveld refined XRD pattern for $x = 0.2$ ($R_p = 10.47\%$, $R_{wp} = 14.18\%$, $R_{exp} = 10.47\%$, G.O.F. = 1.74).

Table 1. Iron content (x) dependence of the cation distribution, oxygen parameter (u), inversion parameter (δ), theoretical lattice parameter (a_{th}), specific surface area (S) and, x-ray density (ρ_{xrd}) of annealed samples of $\text{Co}_{1-x}\text{Fe}_{2+x}\text{O}_4$.

x	Cation Distribution		u (± 0.0017)	δ (± 0.27)	$a_{th}(\text{nm})$ (± 0.0036)	$S(\text{m}^2/\text{g})$ (± 04.10)	$\rho_{xrd}(\text{kg}/\text{m}^3)$ (± 12.15)
	<i>A site</i>	<i>B site</i>					
0.0	$(\text{Co}^{2+}_{0.23}\text{Fe}^{3+}_{0.77})$	$[\text{Co}^{2+}_{0.77}\text{Fe}^{3+}_{1.23}]$	0.3803	0.77	0.8414	25.59	5297.48
0.1	$(\text{Co}^{2+}_{0.00}\text{Fe}^{3+}_{1.00})$	$[\text{Co}^{2+}_{0.09}\text{Fe}^{3+}_{1.10}]$	0.3789	1.00	0.8399	25.81	5292.62
0.15	$(\text{Co}^{2+}_{0.17}\text{Fe}^{3+}_{0.83})$	$[\text{Co}^{2+}_{0.68}\text{Fe}^{3+}_{1.32}]$	0.3799	0.83	0.8393	26.32	5292.86
0.2	$(\text{Co}^{2+}_{0.04}\text{Fe}^{3+}_{0.96})$	$[\text{Co}^{2+}_{0.76}\text{Fe}^{3+}_{1.24}]$	0.3789	0.96	0.8386	29.74	5263.56
0.25	$(\text{Co}^{2+}_{0.75}\text{Fe}^{3+}_{0.25})$	$[\text{Co}^{2+}_{0.00}\text{Fe}^{3+}_{2.00}]$	0.3834	0.25	0.8383	25.35	5272.17
0.4	$(\text{Co}^{2+}_{0.60}\text{Fe}^{3+}_{0.40})$	$[\text{Co}^{2+}_{0.00}\text{Fe}^{3+}_{2.00}]$	0.3827	0.40	0.8362	29.87	5282.03
0.6	$(\text{Co}^{2+}_{0.40}\text{Fe}^{3+}_{0.60})$	$[\text{Co}^{2+}_{0.00}\text{Fe}^{3+}_{2.00}]$	0.3815	0.60	0.8335	36.08	5273.28
0.8	$(\text{Co}^{2+}_{0.08}\text{Fe}^{3+}_{0.92})$	$[\text{Co}^{2+}_{0.12}\text{Fe}^{3+}_{1.88}]$	0.3797	0.92	0.8306	33.90	5289.52

ferrite as well as oxygen parameter (u), and shows cationic distribution alteration as compared to earlier results [14]. Obtained oxygen parameter (u) range between 0.3789 - 0.3834, which is greater than its ideal value $u_{ideal} = 0.375$ [1], is used to quantitative measurement of oxygen distortion in the structure and, its enhancement suggests higher structural disorder.

Figure 3 (a) illustrates Fe^{3+} content dependence of bond angles ($\theta_1, \theta_2, \theta_3, \theta_4, \theta_5$), which are closely related to the strength of A-O-B, B-O-B and, A-O-A super-exchange interaction [1]. Perusal of figure 3 (a) reveal that increase of Fe-content of B-B interaction is strengthened, while weakening of A-B, A-A interaction weakens, which will have effect on magnetic properties, as was also observed earlier [14]. Linear variation of oxygen parameter (u) with inversion parameter (δ) (see fig. 3 (b)) reveal variation of disorder, as observed in [14, 32]. Using figure 3 (b), following experimental relation can be written: $u = 0.38507 - 0.00615 [\delta]$, showing strong connection between u and δ .

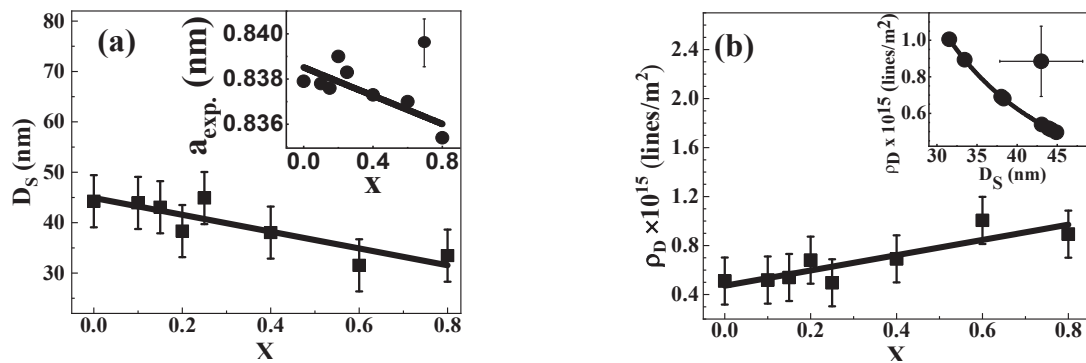


Figure 2. (a) Dependence of D_s with Fe content, Inset: Dependence of $a_{exp.}$ with Fe content, error bar (s) are also shown. (b) Variation of ρ_D with Fe content, Inset: D_s dependence of ρ_D , error bar is also shown. Continuous lines: fit to data.

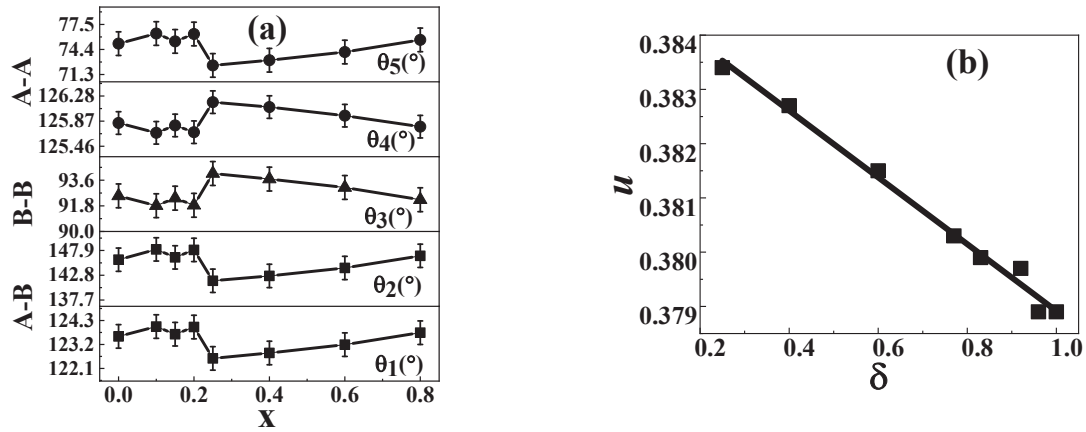


Figure 3. (a) Fe content dependence of bond angles (θ_1^{A-O-B} , θ_2^{A-O-B} , θ_3^{B-O-B} , θ_4^{B-O-B} , θ_5^{A-O-A}). Line connecting points are guide to eye. Error in the estimation of bond angles range between $\pm 0.18 - \pm 2.40$ degree, (b) Variation of u with δ . Continuous line is linear fit.

Figure 4 (a) depicts the hysteresis loops, and its perusal of reveal noticeable considerable changes in hysteresis loops with varying Fe-content, and is reflected in magnetic parameters, given in table 2. Inset of figure 4(a) reveal dependence of $M_{S(exp.)}$ on α_{Y-K} . Perusal of figure 4(a) inset shows linear decrease of saturation magnetization ' $M_{S(exp.)}$ ' with increasing canting angle ' α_{Y-K} ', as was also observed in earlier work on samples without ant post-preparation thermal treatment [14]. Based on figure 4 (a) inset, following experimental relation can be written:

$M_{S(exp.)} = 93.22 - 1.06 [\alpha_{Y-K}]$, reveal correlation between structural (α_{Y-K}), and magnetic properties. Observed behavior in figure 4(a) inset shows that magnetization is described by three sub-lattice model given by Yafet-Kittel [14, 33,], and the saturation magnetization reduction is because of surface spin disorder in spinel nano particles.

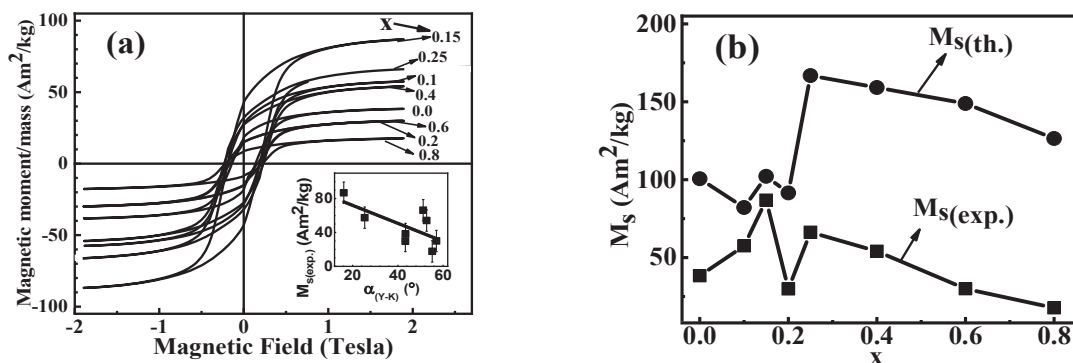


Figure 4. (a) Hysteresis loops of $Co_{1-x}Fe_{2+x}O_4$ ($x=0.0-0.8$) samples, Inset: dependence of $M_{S(exp.)}$ on α_{Y-K} , linear fit is shown by continuous line, (b) Dependence of $M_{S(exp.)}$ and $M_{S(th.)}$ on x , line connecting points are guide to the eye.

Table 2. Iron content (x) dependence of coercivity (H_c), remanence (M_r), experimental saturation magnetization ($M_{S(exp.)}$), theoretical magnetization at 0K ($M_{S(th.)}$), squareness ratio (M_r/M_s), canting angle (α_{Y-K}), Anisotropy constant (K_1) of the studies of $Co_{1-x}Fe_{2+x}O_4$ samples.

x	Sample composition	H_c (Oe) (± 0.0325)	M_r (Am ² /Kg) (± 11.14)	$M_{S(exp.)}$ (Am ² /Kg) (± 22.79)	$M_{S(th.)}$ (Am ² /Kg) (± 32.74)	$M_r/M_{S(exp.)}$ (± 0.009)	(α_{Y-K}) (Degree) (± 14.84)	$K_1 \times 10^4$ (erg/cc) (± 02.71)
0.0	$Co_1Fe_2O_4$	1394.7	18.26	38.30	100.61	0.476	43.37	2.89
0.1	$Co_{0.9}Fe_{2.1}O_4$	1893.3	28.13	57.48	082.13	0.489	25.32	5.88
0.15	$Co_{0.85}Fe_{2.15}O_4$	1895.8	42.68	86.88	102.15	0.492	16.06	8.90
0.2	$Co_{0.8}Fe_{2.2}O_4$	1628.4	15.11	29.88	091.49	0.506	43.29	2.61
0.25	$Co_{0.75}Fe_{2.25}O_4$	2325.0	32.05	66.26	166.83	0.484	51.14	8.29
0.4	$Co_{0.6}Fe_{2.4}O_4$	2284.4	27.13	54.11	159.13	0.501	52.69	6.66
0.6	$Co_{0.4}Fe_{2.6}O_4$	1984.3	14.80	29.97	148.87	0.494	56.98	3.20
0.8	$Co_{0.2}Fe_{2.8}O_4$	2210.7	8.66	17.72	126.45	0.489	55.155	2.11

Figure 4(b) elucidates variation of $M_{S(exp.)}$, $M_{S(th.)}$ with varying Fe-content. Non - similar trend of $M_{S(exp.)}$, $M_{S(th.)}$ observed, shows that magnetization behavior is directed by three sub lattice model [14, 33], as explained earlier. Table 2 shows that obtained H_c values are consistent with computed K_1 values. Obtained H_c values, equivalent grain size (range between: 31.54 – 44.89 nm) suggest that studied ferrites are in single-multi domain overlap regions [34]. Obtained M_r/M_s between 0.27 – 0.47, indicates variation of inter-grain interaction, and isotropic behavior of multi domain grains, and does not have favored magnetization direction is consistent with literature [24, 27, 35].

Figure 5 (a) depicts the representative TAUC plot for $x=0.4$ sample, while figure 5 (a) inset shows variation of bandgap with $a_{exp.}$. Based on figure 5 (a) inset, the following experimental relation is written: Bandgap = 75.10 - 87.93 [$a_{exp.}$], show relationship among bandgap, structural changes i. e. $a_{exp.}$ alteration due to variation of Fe^{3+} content, and bandgap, as was also reported in [14, 15]. Figure 5 (b) depicts the Fe-content dependence of bandgap. Perusal of figure 5 (b), shows exponential increase of bandgap with increase in Fe-content, attributable to variation of cationic distribution (*changes in Fe^{3+} , Co^{2+} ions on A, B site*) [15, 16, 36, 37], and using figure 5 (b) following experimental relation can be

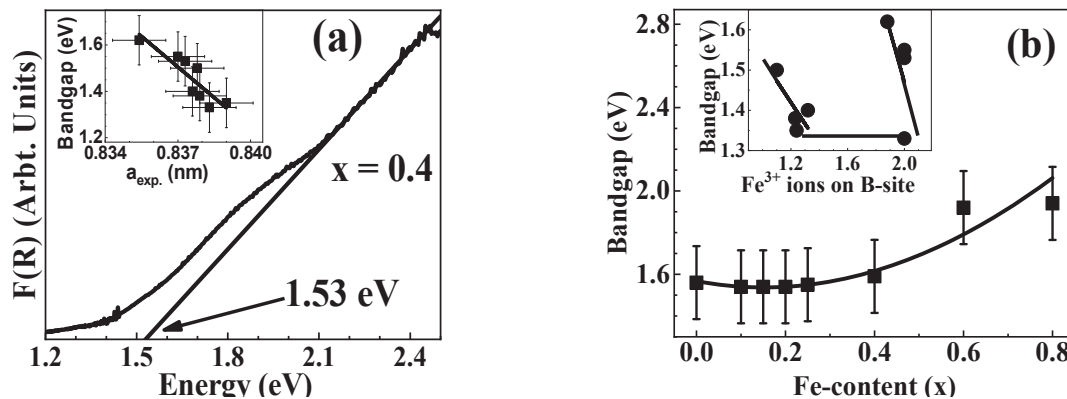


Figure 5. (a) Representative TAUC plot for $Co_{0.9}Fe_{2.1}O_4$ sample ($x=0.4$), Inset: bandgap variation on $a_{exp.}$, continuous line is linear fit), (b) Fe content (x) dependence of bandgap for the studied $Co_{1-x}Fe_{2+x}O_4$ samples, continuous line is exponential fit to the data; Inset: Variation of bandgap with Fe^{3+} on B-site, continuous lines are guide to eye.

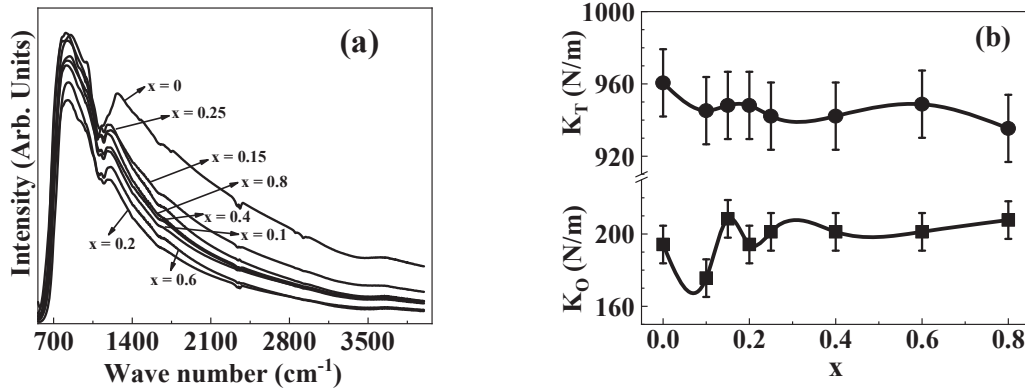


Figure 6. (a) FTIR data of studied $\text{Co}_{1-x}\text{Fe}_{2+x}\text{O}_4$ ($x=0.0-0.8$) samples, (b) Variation of tetrahedral force constant K_T and octahedral force constant K_O with Fe content for the studied sample.

written: $\text{Bandgap} = 65.24 \exp(-[\text{Fe-content}] / 4.92) - 63.67 + 12.86 [\text{Fe-content}]$. Figure 5 (b) clearly shows that the variation of Fe-content in the studied ferrites, can be used for fine-tuning of the bandgap (range between 1.35 eV to 1.5 eV) useful semiconductor device fabrication. Aforementioned explanation of figure 5 (a) inset, is understood in terms of variation of cationic distribution, and figure 5 (b) inset, depicts the bandgap dependence of B-site Fe^{3+} ions, corroborate with the cationic distribution dependence of bandgap, and explained as follows: perusal of figure 5 (b) inset shows that Fe^{3+} ions occupancy on B-site up to 1.33 the bandgap and shows sharp linear decrease, beyond 1.33, and till 1.98 it is almost constant; and beyond 1.98 again a sharp linear increase of bandgap is observed, showing strong correlation between structural properties, and bandgap.

FTIR spectra of the studied $\text{Co}_{1-x}\text{Fe}_{2+x}\text{O}_4$ samples are depicted in Figure 6 (a), while absorption bands (ν_1 , ν_2), tetrahedral (K_T), octahedral (K_O) force constants, and Debye temperature (θ_D) are depicted in table 3. FTIR spectra reveal two main characteristic absorption bands of spinel crystal lattice in the frequency range 500- 4000 cm^{-1} : the first one is high frequency ' ν_1 ' is in the range 800–853 cm^{-1} , while the second one is low frequency ' ν_2 ' is in the range 482–504 cm^{-1} as was also reported in [14, 38]. These bands ν_1 , ν_2 are ascribed respectively to vibrations of MeA-O and MeB-O vibrations. The difference in the band positions of ν_1 and ν_2 as a function of Fe-content is ascribable to the variation in the distances of the MeA-O, and MeB-O complexes respectively [14, 39]. It is found that minor shift of band positions with the function of Fe-content (see table 3) are attributable to the

Table 3. Iron content (x) dependence of IR absorption bands, (K_T and K_O) force constants and Debye temperature (θ_D) of annealed samples of $\text{Co}_{1-x}\text{Fe}_{2+x}\text{O}_4$.

x	Sample composition	Tetrahedral complex ν_1 (cm^{-1})	Octahedral complex ν_2 (cm^{-1})	K_T (N/m) (± 18.6)	K_O (N/m) (± 10.4)	θ_D (K) (± 07.3)
0.0	$\text{Co}_1\text{Fe}_2\text{O}_4$	852.6	486.3	530.7	194.2	960.6
0.1	$\text{Co}_{0.9}\text{Fe}_{2.1}\text{O}_4$	835.2	482.2	507.8	175.6	945.2
0.15	$\text{Co}_{0.85}\text{Fe}_{2.15}\text{O}_4$	817.7	503.8	487.8	208.4	948.1
0.2	$\text{Co}_{0.8}\text{Fe}_{2.2}\text{O}_4$	835.6	486.3	508.0	194.2	948.1
0.25	$\text{Co}_{0.75}\text{Fe}_{2.25}\text{O}_4$	817.7	495.6	491.1	201.2	942.2
0.4	$\text{Co}_{0.6}\text{Fe}_{2.4}\text{O}_4$	817.7	495.6	490.3	201.2	942.2
0.6	$\text{Co}_{0.4}\text{Fe}_{2.6}\text{O}_4$	826.9	495.6	500.3	201.2	948.8
0.8	$\text{Co}_{0.2}\text{Fe}_{2.8}\text{O}_4$	800.3	503.4	466.7	207.7	935.4

variation of ionic distances FeB-O, and FeA-O [14, 40], explains the stronger covalent bonding of Fe^{3+} ions at the tetrahedral than at octahedral sites. Perusal of table 3, figure 5 (b) depicts that the K_T decreases (for the studied thermally annealed samples, with increasing Fe content) is found to increase as a_{exp} decreases, suggests the strengthening of inter-atomic bonding, while the force constants K_O is found to increase as a_{exp} decreases, shows inter-atomic bond weakening [14, 38]. Perusal of table 3 shows that Debye temperature (θ_D) decreases with increasing Fe-content, suggests variation of lattice vibrations, and agrees well with the values reported in literature [14, 40].

4. Summary

Nanocrystalline spinel $\text{Co}_{1-x}\text{Fe}_{2+x}\text{O}_4$ ferrites were prepared via sol gel autocombustion technique. Formation of spinel phase is validated by XRD. Results reveal modification of – lattice parameter, dislocation density, cationic distribution, degree of inversion, A–A, B–B, A–B, super-exchange interactions, saturation magnetization, coercivity, anisotropy, bandgap, and lattice vibrations. Current work noticeably reveal strong connection between structural properties, bandgap, and magnetic properties.

Acknowledgments

Authors thank Dr. M Gupta, and Dr. U. P. Deshpande, UGC-DAE CSR, Indore for respectively for XRD, and UV-Vis, FTIR measurements. One month hospitality to S. N. Kane, during June 2018 as invited professor at Ecole Normale Supérieure de Cachan, University Paris-Saclay, Cachan (France), gratefully acknowledged.

References

- [1] Smit J and Wijn H P J 1959 *Ferites* (Eindhoven, The Netherlands: Philips Technical Library)
- [2] Sertkol M, Köseoglu Y, Baykal A, Kavas H and Toprak M S 2010 *J. Magn. Magn. Mater.* **322** 866-71
- [3] Costa A C F M, Silva V J, Cornejo D R, Morelli M R, Kiminami R H G A and L. Gama 2008 *J. Magn. Magn. Mater.* **320** e370-72
- [4] Willard M A, Kurihara L K, Carpenter E E, Calvin S and Harris V G 2004 *Int. Mater. Rev.* **49** 125-70
- [5] Shanmugavel T, Gokul Raj S, Rajarajan G and Ramesh Kumar G 2014 *Procedia Mater. Sci.* **6** 1725-30
- [6] Satalkar M, Kane S N, Ghosh A, Ghodke N, Barrera G, Calegato F, Coisson M, Tiberto P and Vinai F 2014 *J. Alloys Comp.* **615** S313-16
- [7] Panchal S, Raghuvanshi S, Gehlot K, Mazaleyrat F and Kane S N 2016 *AIP Adv.* **6** 055930-1-6
- [8] Feng X, Huang Y, Chen X, Wei C, Zhang X and Chen M 2018 *J. Mater. Sci.* **53** 2648–57
- [9] Chen D H and He X R 2001 *Mater. Res. Bull.* **36** 1369–77
- [10] Wang X, Hou X, Mao J, Gao Y, Ru Q, Hu S and LamKh 2016 *J. Mater. Sci.* **51** 5843–56
- [11] Barrera G, Coisson M, Calegato F, Raghuvanshi S, Mazaleyrat F, Kane S N and Tiberto P 2018 *J. Magn. Magn. Mater.* **456** 372–80
- [12] Raghuvanshi S, Mazaleyrat F and Kane S N 2018 *AIP Adv.* **8** 047804-1-11
- [13] Raghuvanshi S, Tiwari P, Kane S N, Avasthi D K, Mazaleyrat F, Tatarchuk T and Mironyuk I 2019 *J. Magn. Magn. Mater.* **47** 521-28
- [14] Kane S N, Tiwari P, Deepti, Verma R, Deshpande U P and Mazaleyrat F 2020 *Mater. Today: Proc.* **32** 358-64
- [15] Verma R, Mazaleyrat F, Deshpande U P and Kane S N 2020 *Mater Today Proc.* **32** 329–33
- [16] Devi E C and Soibam I 2018 *J. Supercond. Nov Magn.* **31** 1183–88
- [17] Cedeno-Mattei Y, Perales-Perez O, Uwakweh O N C and Xin Y 2010 *J. Appl. Phys.* **107** 09A741-1-3
- [18] Na H B, Song I C and Hyeon T 2009 *Adv. Mater.* **21** 2133-48
- [19] Ahmad T, Rhee I, Hong S, Chang Y and Lee J 2011 *J. Nanosci. Nanotech.* **11** 5645-50

- [20] Zhang W, Zuo X, Niu Y, Wu C, Wang S, Gun S and Silva S R P 2017 *Nanoscale* **9** 3929-37
- [21] Kharabe R G, Devan R S, Kanamadi C M and Chougule B K 2006 *Smart Mater. Struct.* **15** N36-39
- [22] Raghuvanshi S, Kane S N, Lalla N P and Reddy V R 2016 *J. Phys.: Conf. Ser.* **755** 012049-1-5
- [23] Kriegisch M, Ren W, Sato-Turtelli R, Muller H, Grossinger R and Zhang Z 2012 *J. Appl. Phys.* **111** 07E308-1-3
- [24] Tiwari P, Verma R, Modak S S, Reddy V R, Mazaleyrat F and Kane S N 2021 *Hyperfine Inter.* **242** 51-1-15
- [25] Lutterotti L and Scardi P 1990 *J. Appl. Cryst.* **23** 246-52
- [26] Verma R, Kane S N, Tiwari P, Modak S S, Tatarchuk T and Mazaleyrat F 2018 *Mol. Cryst. Liq. Cryst.* **674** 130-41
- [27] Verma R, Kane S N, Deshpande U P and Mazaleyrat F 2021 *Mater. Today: Proc.* **46** 2205-11
- [28] Bertaut E F 1950 *Comptes Rendus Hebdomadaires des Seances de l'Academie des Sciences* **230** 213-15
- [29] Kubelka P and Munk F Z 1931 *Tech. Phys.* **12** 593-601
- [30] Mallesh S, Prabu D and Srinivas V 2017 *AIP Adv.* **7** 056103-1-8
- [31] Yadav R S, Kuřitka I, Vilcakova J, Havlica J, Masilko J, Kalina L, Tkacz J, Švec J, Enev V and Hajdúchová M 2017 *Adv. Nat. Sci.: Nanosci. Nanotechnol.* **8** 045002-1-14
- [32] Barrera G, Coisson M, Celegato F, Raghuvanshi S, Mazaleyrat F, Kane S N and Tiberto P 2018 *J. Magn. Mgn. Mater.* **456** 372-80
- [33] Murthy N S S, Natera M G, Youssef S I, Begum R J and Srivastava C M 1969 *Phys. Rev.* **181** 969-77
- [34] Kolhatkar A G, Jamison A C, Litvinov D, Willson R C and Lee T R 2013 *Int. J. Mol. Sci.* **14** 15977-16009
- [35] Shirsath S E, Toksha B G and Jadhav K M 2009 *Mater. Chem. Phys.* **117** 163-168
- [36] Chakrabarty S, Pal M and Dutta A 2015 *Mater. Chem. Phys.* **153** 221-28
- [37] Taufiq A, Hidayat A, Sunaryono, Hidayat N and Soontaranon S 2019 *IOP Conf. Series: Mater. Sci. Eng.* **515** 012047-1-11
- [38] Tiwari P, Verma R, Kane S N, Tatarchuk T and Mazaleyrat F 2019 *Mater. Chem. Phys.* **229** 78-86
- [39] Zipare K V, Bandgar S S and Shahane G S 2018 *J. Rare Earths* **36** 86-94
- [40] Modi K B, Raval P Y, Shah S J, Kathad C R, Dulera S V, Popat M V, Zankat K B, Saija K G, Pathak T K, Vasoya N H, Lakhani V K, Chandra U and Jha P K 2015 *Inorg. Chem.* **54** 1543-55